The Astrophysical Journal, 720:1603–1611, 2010 September 10 doi:10.1088/0004-637X/720/2/1603

PARTICLE ACCELERATION IN FRAGMENTING PERIODIC RECONNECTING CURRENT SHEETS IN SOLAR FLARES

M. Gordovskyy, P. K. Browning, and G. E. Vekstein
Jodrell Bank Centre for Astrophysics, School of Physics and Astronomy, University of Manchester, Manchester M13 9PL, UK;
mykola.gordovskyy@manchester.ac.uk
Received 2010 June 8; accepted 2010 July 1; published 2010 August 25

ABSTRACT

Proton and electron acceleration in a fragmenting periodic current sheet (CS) is investigated, based on the forced magnetic reconnection scenario. The aim is to understand the role of CS fragmentation in high-energy beam generation in solar flares. We combine magnetohydrodynamics and test-particle models to consider particle trajectories consistent with a time-dependent reconnection model. It is shown that accelerated particles in such a model form two distinct populations. Protons and electrons moving in open magnetic field have energy spectra that are a combination of the initial Maxwellian distribution and a power-law high-energy ($E > 20$ keV) part. The second population contains particles moving in a closed magnetic field around O-points. These particles move predominantly along the guiding field and their energies fall within quite a narrow range between ∼1 MeV and ∼10 MeV. It is also found that particles moving in an open magnetic field have a considerably wider pitch-angle distribution.

Key words: acceleration of particles – magnetic reconnection – Sun: flares

Online-only material: color figures

1. INTRODUCTION

Particle acceleration is one of the main phenomena associated with solar flares and other explosive events in the corona. Observations show that in major events electrons can be accelerated to tens of MeV while ions gain energies up to several GeV, and high-energy particles may carry up to ∼30% of the flare energy budget (see Aschwanden 2002; Lin 2008; Klein & MacKinnon 2007, for reviews). It is generally accepted that magnetic reconnection is responsible for the fast energy release in flares. However, the processes behind particle acceleration are much less understood. Several effective mechanisms have been proposed, but a comprehensive model allowing satisfactory interpretation of most observational features is far from being complete.

Most theories utilize one of the following mechanisms: acceleration by direct electric field, energization through wave-particle interaction, acceleration at shock fronts, and *Fermi* acceleration in collapsing magnetic traps, or a combination of different mechanisms (see Benz 2008; Vlahos et al. 2009, and references therein). There is no general agreement on which of the mechanisms is most important in flares. However, since magnetic reconnection is associated with strong electric currents, particle acceleration by direct electric fields is unavoidable, at least at the primary energy release site in the corona.

A basic model of charged particle motion in current sheets (CSs) has been considered by Speiser (1965). Later this type of acceleration was studied analytically in simple CS configurations (Martens & Young 1990; Litvinenko & Somov 1993; Zhu & Parks 1993) and numerically in more advanced CS models (Sato et al. 1982; Kliem 1994; Heerikhuisen et al. 2002; Wood & Neukirch 2005). Nearly all modeling has focused on steady reconnection. However, flares are clearly transient events and it is important to understand how particle energization evolves through such an event. Recently, Gordovskyy et al. 2010 (Paper I, hereafter) combined magnetohydrodynamics (MHD) and test-particle methods to investigate proton and electron motion in a time-dependent CS model based on the forced reconnection scenario (Hahm & Kulsrud 1985; Vekstein & Jain 1998; Jain et al. 2005). In this scenario, CS formation and subsequent reconnection are triggered by an external disturbance. It is shown that protons and electrons can be accelerated to energies of at least tens of MeV and can be ejected in different directions (similar to Zharkova & Gordovskyy 2004). In that model, particles are most effectively accelerated near the magnetic X-point while additional acceleration (though less effective) occurs due to the current formed in the outflow region around magnetic islands. A similar effect has been observed by Oka et al. (2010) in a model with two interacting magnetic O-points.

While most studies focus on a single monolithic CS configuration, the acceleration in a fragmented CS (with regular or chaotic structure) may be important. A fragmented CS may be more effective than a monolithic sheet or null point for accelerating large numbers of particles (Vlahos et al. 2009). Indeed, such a fragmentation of the CS may occur naturally due to the tearing instability in the initially long and thin CS or due to external perturbations—which are likely to be common in the corona.

In the present paper, we investigate particle motion in a time-dependent CS model, building on the approach developed in Paper I. First, we use MHD simulations in order to study fragmentation of a single infinite CS during the magnetic reconnection triggered by an external boundary displacement. Then proton and electron trajectories are calculated using the test-particle approach based on the relativistic guiding center approximation. The obtained trajectories are used to investigate particle energy spectra, pitch-angle distributions, and directivity of high-energy particle ejection.

2. MODEL OF TRANSIENT MAGNETIC RECONNECTION EVENT

In the present study, we use background fields from 2D3V MHD model of magnetic reconnection developed in Paper I (see Figure 1), which is based on the forced reconnection

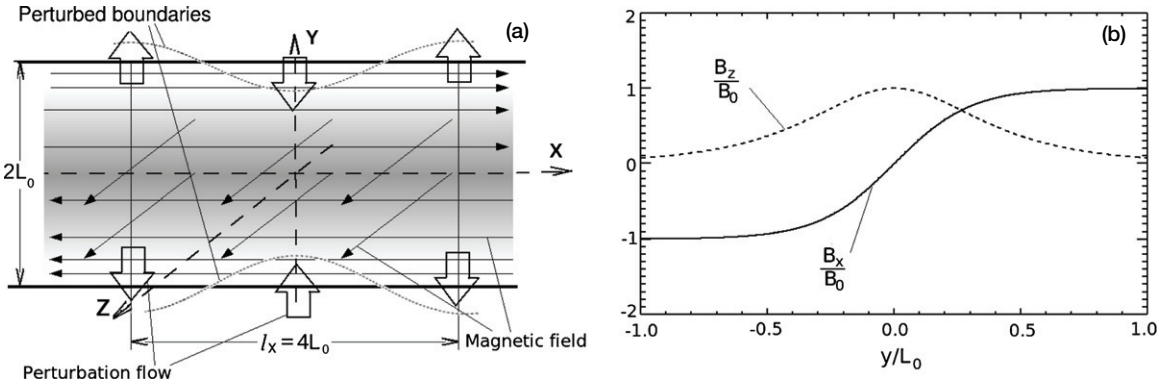

Figure 1. Considered model scheme (a) and the initial magnetic field (b).

model (Hahm & Kulsrud 1985). The model is infinite in the x-direction, invariant in the z-direction, and has upper and lower boundaries at $y = L_0$ and $y = -L_0$, respectively. The initial configuration is a stationary force-free Harris sheet with a magnetic field defined as

$$\vec{B}_{\rm ini} = B_0 \left[\tan h \frac{y}{y_0}; 0; \sec h \frac{y}{y_0} \right], \quad (1)$$

(i.e., $|B| = B_0$), with constant density $\rho_{\rm ini} = \rho_0$ and constant pressure $p_{\rm ini} = 0.01 \frac{B_0^2}{2\mu_0}$ (i.e., it is magnetically dominated, low-β plasma). The local resistivity depends on current density as a step-like function:

$$\eta = \begin{cases} 0 & (j < j_{\rm cr}) \\ \eta_1 & (j \geqslant j_{\rm cr}), \end{cases} \quad (2)$$

i.e., the local resistivity is zero unless the local current density is greater than the critical current $j_{\rm cr}$. In all the simulations, the critical current is greater than the maximum initial current density ($j_{\rm cr} > \max[j(t = 0)]$) and, therefore, initially the resistivity is zero. This resistivity profile represents current-driven anomalous resistivity arising due to microinstability (see Dreher et al. 1997).

The reconnection is triggered by a transient perturbation of the upper and lower boundaries. This is done by applying plasma flows in the following form:

$$v_x = 0$$

$$v_y = \begin{cases} \pm \frac{\Delta}{t_{\rm imp}} \cos\left(\frac{2\pi x}{l_x}\right) \times \\ \left[1 - \cos\left(\frac{2\pi t}{t_{\rm imp}}\right)\right], & t < t_{\rm imp} \\ 0, & t > t_{\rm imp} \end{cases} \quad (3)$$

$$v_z = 0,$$

where l_x is the spatial period in the x-direction, Δ is the amplitude of boundary displacement, and $t_{\rm imp}$ is the duration of perturbation impulse. The sign in the formula for v_y is positive for the lower boundary and negative for the upper boundary. Boundary conditions for the pressure, density, and magnetic field are chosen to ensure that there are no forces and no electric currents perpendicular to the upper and lower boundaries: $\frac{\partial p}{\partial y} = 0$, $\frac{\partial \rho}{\partial y} = 0$, $\frac{\partial B_x}{\partial y} = \frac{\partial B_y}{\partial x}$, $\frac{\partial B_y}{\partial y} = 0$, and $\frac{\partial B_z}{\partial y} = 0$, i.e., after the perturbation impulse ends, the boundary conditions at $y = \pm L_0$ correspond to rigid boundaries. In the corona, such a perturbation can be the result of a photospheric footpoint motion, newly emerging magnetic flux, or an adjacent coronal disturbance.

The evolution of the system can be described using the standard set of resistive MHD equations (e.g., Priest 1982):

$$\frac{\partial \rho}{\partial t} = -\vec{\nabla} \cdot (\rho \vec{v}) \quad (4)$$

$$\frac{\partial \vec{v}}{\partial t} = -(\vec{v} \cdot \vec{\nabla})\vec{v} - \frac{1}{\rho}\vec{j} \times \vec{B} - \frac{1}{\rho}\vec{\nabla} P \quad (5)$$

$$\frac{\partial w}{\partial t} = -(\vec{v} \cdot \vec{\nabla})w - (\gamma - 1) w \, \vec{\nabla} \cdot \vec{v} + \frac{\eta j^2}{\rho} \quad (6)$$

$$\frac{\partial \vec{B}}{\partial t} = \vec{\nabla} \times [\vec{v} \times \vec{B}] - \vec{\nabla} \times (\eta \vec{j}) \quad (7)$$

$$\vec{j} = \frac{1}{\mu_0}[\vec{\nabla} \times \vec{B}], \quad (8)$$

where w is the specific internal energy density related to pressure and density as $p = (\gamma - 1)\rho w$ and μ_0 is the magnetic permeability.

The set of Equations (4)–(8), along with the initial and boundary conditions described above, has been solved numerically using the Lare2D MHD code (Arber et al. 2001) on a uniform 256 × 128 grid. The simulations have been performed for different sets of model parameters. Thus, the resistivity η_1 was varied from 3.2×10^{-4} to 3.3×10^{-3} $\mu_0 L_0 v_0$, where v_0 is the characteristic Alfvén speed $v_0 = \mu_0^{-1/2} B_0 \rho_0^{-1/2}$. The initial CS thickness y_0 was either $0.25\,L_0$ or $0.40\,L_0$. In all the experiments the critical current value was set slightly above the initial current density: $j_{\rm cr} \approx 1.02 \frac{B_0}{\mu_0 y_0}$, i.e., it was $j_{\rm cr} = 4.1 \frac{B_0}{\mu_0 L_0}$ and $2.6 \frac{B_0}{\mu_0 L_0}$ for $y_0 = 0.25\,L_0$ and $0.40\,L_0$, respectively. The spatial period of boundary perturbation is $l_x = 4\,L_0$ and, therefore, the size of the model domain is $4\,L_0$ by $2\,L_0$. The duration of impulse was $t_{\rm imp} = 16 t_0$ (where t_0 is the characteristic Alfvén time $t_0 = L_0/v_0$) and the amplitude of boundary displacement was $\Delta = 0.1$.

Magnetic field, current density, and plasma flow directions from one of the numerical experiments are shown in Figure 2. It can be seen that the CS evolution consists of two main

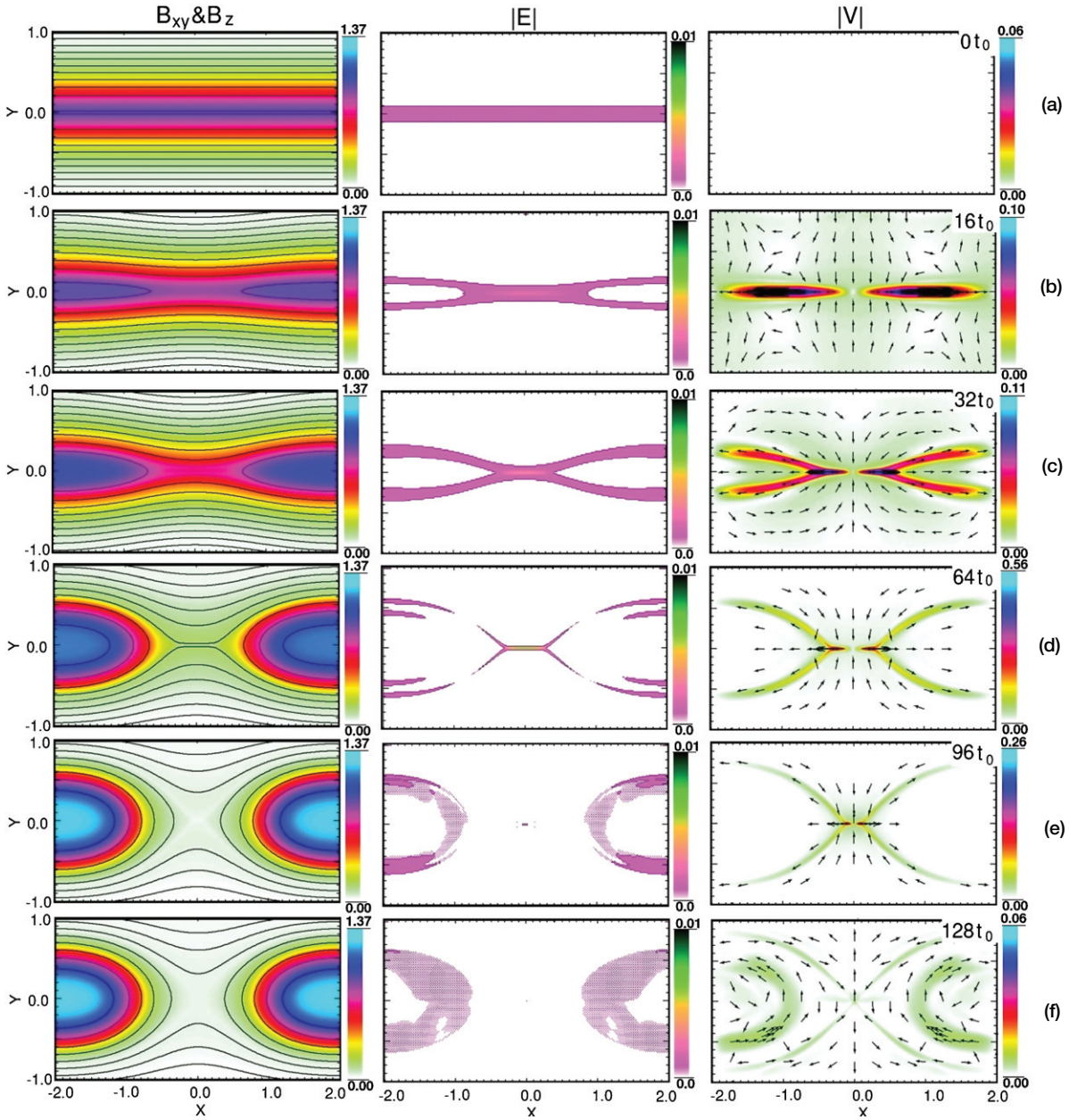

Figure 2. Evolution of magnetic field, current density, and plasma velocity in a transient reconnection event with characteristic CS thickness $y_0 = 0.25\,L_0$ and critical resistivity $\eta_1 = 3.2 \times 10^{-4}\,\mu_0 L_0 v_0$. Left panels show x–y magnetic field lines and B_z distribution as a colorscale. Middle panels show the absolute value of electric field. Right panels show plasma flow direction (black arrows) and absolute value of plasma velocity as the colorscale. The panels correspond to the following times: (a) 0, (b) $16t_0$, (c) $32t_0$, (d) $64t_0$, (e) $96t_0$, and (f) $128t_0$. The colorscale changes between graphs to enhance the contrast.

(A color version of this figure is available in the online journal.)

stages which are broadly consistent with analytical models of forced reconnection (Hahm & Kulsrud 1985) but have more complex dynamics. During the boundary perturbation impulse, the magnetic field is deformed, leading to enhancement of current density around the center of the domain (Figures 2(a) and (b)). When the current density reaches j_{cr}, the reconnection starts in a long and thin diffusion layer, with plasma inflow in the y-direction and outflow in the x-direction. The horizontal size of the CS gradually decreases while plasma outflow becomes organized in four separatrix jets (Figures 2(c) and (d)).

As the field reconnects, magnetic islands start to form in the outflow areas around the O-points. As expected from the analytical theory (Vekstein & Jain 1998), the islands grow, resulting in the concentration of magnetic field and current (Figures 2(e) and (f)). The current density in these regions is much lower than it was in the primary CS, staying close to the value of critical current j_{cr}. When the size of the magnetic islands becomes comparable to the width of the domain ($2L_0$), the reconnection rate reduces to nearly zero and the magnetic field topology and magnetic energy in the domain effectively do not change, indicating that the system is near its final "reconnected" equilibrium.

3. PARTICLE MOTION IN THE MODEL CURRENT SHEET

3.1. Formulation and Numerical Approach

In order to connect the test-particle model with the MHD simulations, the scaling parameters L_0, B_0, and ρ_0 have to be

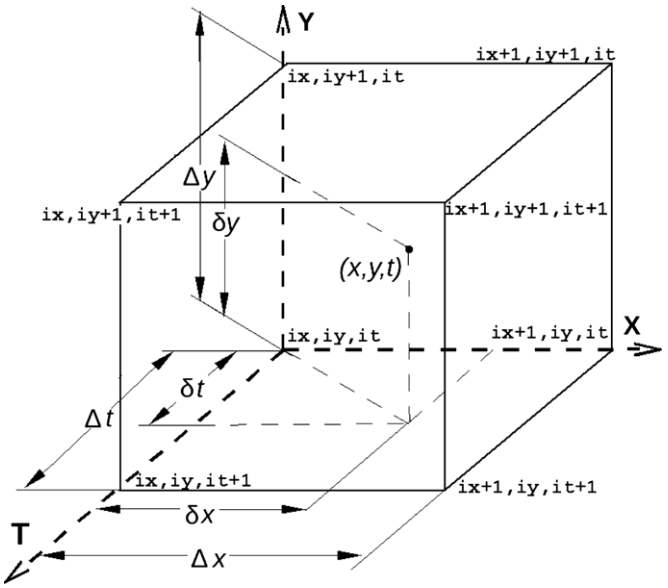

Figure 3. Particle coordinates in a cell of neighboring grid points.

defined. The adopted characteristic scale length in our MHD model is $L_0 = 10^4$ m. This yields $\sim 10^4$ m for the width of the CS (in x-direction) and about 10^2–10^3 m for CS thickness (in y-direction). The characteristic magnetic field is $B_0 = 3 \times 10^{-3}$ T and characteristic density is $\rho = 4 \times 10^{-12}$ kg m^{-3} (corresponding to the particle density 2.4×10^9 cm^{-3}. These values are chosen to match the typical coronal CS. Based on these values one can deduce the characteristic Alfvén velocity $v_0 = 1.34 \times 10^6$ m s^{-1}, characteristic Alfvén time $t_0 = 7.6 \times 10^{-3}$ s, and initial temperature (assuming fully ionized hydrogen plasma) $T_0 = 0.02 \frac{m_p}{k_B \mu_0} \frac{B_0^2}{\rho_0} \approx 2.2 \times 10^6$ K.

Provided that the magnetic field is always larger than 0.01 B_0, the gyro-radii for protons with thermal energies ($\sim$1 keV) will be at least $\sim 10^{-4} L_0$ and, obviously, much smaller for electrons (see Table 1 in Paper I). Therefore, the guiding center approximation is valid in this case. We study particle trajectories using the following set of relativistic guiding center equations of motion (Northrop 1963):

$$\frac{d\mathbf{r}}{dt} = \mathbf{u} + \frac{\gamma(v_{||})}{\gamma}\mathbf{b} \tag{9}$$

$$\begin{aligned}\mathbf{u} = \mathbf{u}_E &+ \frac{m}{q}\frac{(\gamma v_{||})^2}{\gamma \kappa^2 B}[\mathbf{b} \times (\mathbf{b} \cdot \nabla)\mathbf{b}] + \frac{m}{q}\frac{\mu}{\gamma \kappa^2 B}[\mathbf{b} \times (\nabla(\kappa B))] \\ &+ \frac{m}{q}\frac{(\gamma v_{||})}{\kappa^2 B}[\mathbf{b} \times (\mathbf{b} \cdot \nabla)\mathbf{u}_E] + \frac{m}{q}\frac{(\gamma v_{||})}{\kappa^2 B}[\mathbf{b} \times (\mathbf{u}_E \cdot \nabla)\mathbf{b}] \\ &+ \frac{m}{q}\frac{\gamma}{\kappa^2 B}[\mathbf{b} \times (\mathbf{u}_E \cdot \nabla)\mathbf{u}_E] + \frac{1}{\gamma c^2}\frac{E_{||}}{\kappa^2 B}(\gamma v_{||})[\mathbf{b} \times \mathbf{u}_E]\end{aligned} \tag{10}$$

$$\begin{aligned}\frac{d(\gamma v_{||})}{dt} = &\frac{q}{m}\mathbf{E} \cdot \mathbf{b} - \frac{\mu}{\gamma}(\mathbf{b} \cdot \nabla(\kappa B)) + (\gamma v_{||})\mathbf{u}_E \cdot ((\mathbf{b} \cdot \nabla)\mathbf{b}) \\ &+ \gamma \mathbf{u}_E \cdot ((\mathbf{u}_E \cdot \nabla)\mathbf{b})\end{aligned} \tag{11}$$

$$\gamma = \sqrt{\frac{c^2 + (\gamma v_{||})^2 + 2\mu B}{c^2 - u^2}} \tag{12}$$

$$\frac{d\mu}{dt} = 0. \tag{13}$$

Here, $\mathbf{r}(t)$ is the position vector, $\mathbf{u}$ is the particle drift velocity perpendicular to the magnetic field, $v_{||}$ is the particle velocity parallel to the magnetic field, $\mathbf{u}_E = \frac{\mathbf{E} \times \mathbf{b}}{B}$ is the local $E \times B$ drift velocity, and $\mathbf{b}$ is the magnetic field direction vector $\mathbf{b} = \mathbf{B}/B$. Also, γ is the relativistic factor, $\gamma = \frac{c}{\sqrt{c^2 - v^2}}$, where v is the absolute particle velocity and κ is the coefficient reducing the field value to the particle frame of reference, $\kappa = \sqrt{1 - u_E^2/c^2}$. Finally, μ is the particle magnetic moment, $\mu = \frac{u_g^2}{2B}$.

The numerical approach used in the present work is a further development of that used in Paper I with two principal differences. First, in the present work particles are moving in time-dependent electric and magnetic fields, while in Paper I particle trajectories were investigated using a quasi-static approach. (In other words, in Paper I trajectories were calculated for a series of background field snapshots, assuming the field is constant in every snapshot, while in the present model the field is updated in time as the particles move.) This is particularly important for protons, which have acceleration times of $\sim 10 t_0$, i.e., comparable to the characteristic timescale of reconnecting current sheet (RCS) evolution (Section 3.2). Second, the particle trajectories are now studied taking into account relativistic effects, which might be particularly important for fast electrons. In addition, in the present model we follow the evolution of a single particle population (both for protons and electrons) rather than adding a new set of test particles for every new background field snapshot.

In every experiment, initially there are $\sim 10^6$ test particles which are uniformly distributed in the phase space of x, y, initial speed $v_f = \sqrt{v_{||}^2 + v_g^2}$, and pitch angle v_g/v_f. There are 64 positions in the x-direction (from $-2\,L_0$ to $2\,L_0$), 32 positions in the y-direction (from $-L_0$ to L_0), 64 positions along the velocity axis (in the range from 0 to $\sim 6 v_{\rm th}$, where $v_{\rm th} = \sqrt{2 k_B T_0/m}$), and eight positions with different pitch angles (from -1 to 1). Each test particle is assigned a statistical weight w depending on the initial full particle velocity as $w = v_f^2 \exp(-v_f^2/v_{\rm th}^2)$. This weight is taken into account in the statistical analysis of the particle population (e.g., in the energy spectra calculations) and, hence, the initial energy spectrum is Maxwellian, corresponding to the temperature T_0.

The trajectory for each test particle is calculated using Equations (9)–(13) with the electric and magnetic fields and their derivatives being determined using simple linear interpolation between grid points and time snapshots taken from the MHD simulations (Section 2):

$$\begin{aligned}F(x_p, y_p, t_p) = (1 - s_t)\,&[(1 - s_x)(1 - s_y) f_{ix,iy,it} \\ &+ s_x(1 - s_y) f_{ix+1,iy,it} + (1 - s_x) s_y f_{ix,iy+1,it} \\ &+ s_x s_y f_{ix+1,iy+1,it}] + s_t\ [(1 - s_x) \\ &\times (1 - s_y) f_{ix,iy,it+1} + s_x(1 - s_y) f_{ix+1,iy,it+1} \\ &+ (1 - s_x) s_y f_{ix,iy+1,it+1} + s_x s_y f_{ix+1,iy+1,it+1}],\end{aligned} \tag{14}$$

where F is the sought value (i.e., one of the fields at the location (x_p, y_p) and time t_p), f denotes this field defined on the three-dimensional numerical grid (two coordinates and time), s_x, s_y, and s_t are the normalized coordinates of (x_p, y_p, t_p) within the

cell of neighboring grid points (see Figure 3):

$$s_x = \frac{\delta x}{\Delta x} = \frac{x_p - x_{ix}}{x_{ix+1} - x_{ix}}$$
$$s_y = \frac{\delta y}{\Delta y} = \frac{y_p - y_{iy}}{y_{iy+1} - y_{iy}}$$
$$s_t = \frac{\delta t}{\Delta t} = \frac{t_p - t_{it}}{t_{it+1} - t_{it}}.$$

Here, $\Delta x = x_{ix+1} - x_{ix}$ and $\Delta y = y_{iy+1} - y_{iy}$ are the grid steps in the x- and y-directions (both equal $1.5625 \times 10^{-2}\, L_0$, see Section 2) and $\Delta t = t_{it+1} - t_{it}$ is the time step of the MHD model output (in all the simulations $\Delta t = 2t_0$). The calculation runs until $256t_0$ unless the test particle leaves the domain earlier through one of the boundaries $y = \pm L_0$.

3.2. Proton and Electron Trajectories

Several test-particle trajectories are plotted in Figures 4 and 5 for protons and electrons, respectively. It can be seen that both types of particles predominantly follow the magnetic field lines, as expected. The reconnection process leads to formation of the two magnetic field regions: the "open" field lines near the upper and lower boundaries and "closed" field lines of magnetic islands in the outflow regions. This, in turn, results in two distinct types of particle trajectories. Thus, protons and electrons in an open magnetic field (blue, red, and orange lines in Figure 4 and all but green lines in Figure 5) travel rather long distances in the x-direction while oscillating in the y-direction. At the same time, there are protons and electrons trapped in the magnetic islands (pink, brown, green, and black lines in Figure 4 and green line in Figure 5) rotating in the x–y plane. Both types of particles have significant velocity in the z-direction. However, while protons and electrons have out-of-plane (v_z) velocities comparable to their in-plane ($\sqrt{v_x^2 + v_x^2}$) velocities, particles trapped in the magnetic islands have substantially higher v_z velocities.

This results in quite an interesting distribution of particles in space at the end of reconnection (Figures 6 and 7). The majority of particles move along open field lines (blue triangles in Figures 6 and 7) with relatively small v_z velocities and, hence, stay very close to $z = 0$. At the same time, a small number of particles (~10% of total number) rotating around magnetic islands (red crosses in Figures 6 and 7) have very high v_z velocities (~1–10 v_0 for protons and ~10–10^4 v_0 for electrons) and form column-like structures in x–y–z space. This behavior can be easily explained by the magnetic field topology: during the reconnection, the z-component of magnetic field (i.e., guiding field) becomes concentrated in the magnetic islands while its magnitude in the inflow region is reduced by a factor of ~10 (see left panels in Figure 2).

The two populations can exchange particles. Particles from the open magnetic field are trapped due to the inflow–outflow drift close to the X-point. At the same time, the presence of a small number of particles with large z in the open field indicates that they can also escape from the magnetic islands into the open field. Most likely, it happens due to $E \times B$ drift with bulk plasma flow. Indeed, there is no free outflow in this closed MHD model and during magnetic reconnection the plasma from the outflow region should drift back into the inflow region (Figure 2, also see Paper I for details).

Electrons are accelerated on characteristic timescales of ~1–10t_0, while for protons this time is ~10–100t_0 and this results in a different "acceleration pattern." The energy of

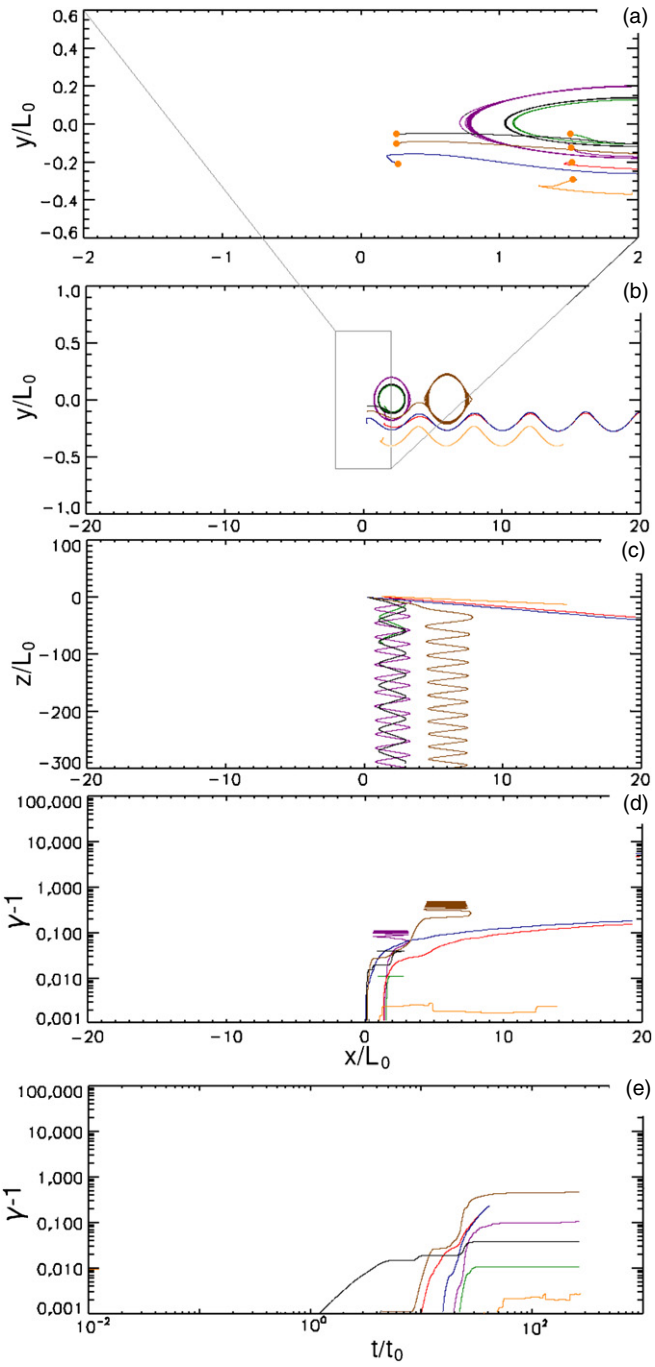

Figure 4. Typical proton trajectories. The initial particle positions are shown by yellow dots. All particles initially have parallel velocities of $v_{||} = 0.1\, v_0$ and pitch angles $u_g/v_{||} = 1.0$. Magnetic and electric fields are taken from the model with $y_0 = 0.25\, L_0$ and $\eta_1 = 3.2 \times 10^{-4}\, \mu_0 L_0 v_0$ (see Figure 2). Panels (a) and (b) show x–y projection of the trajectories, (c) x–z projection of the trajectories, (d) particle energies vs. distance x, (e) particle energies vs. time.

(A color version of this figure is available in the online journal.)

electrons in the open field increases with time in a step-like manner, jumping up when a particle is passing close to the X-point. During proton acceleration the CS undergoes significant changes and electric field distribution becomes more diffuse. As a result, the energy of protons in open field increases with time smoothly without noticeable jumps.

Protons and electrons trapped in magnetic islands show more monotonic energy gain and slightly longer acceleration times compared with the same species in open field. This is because

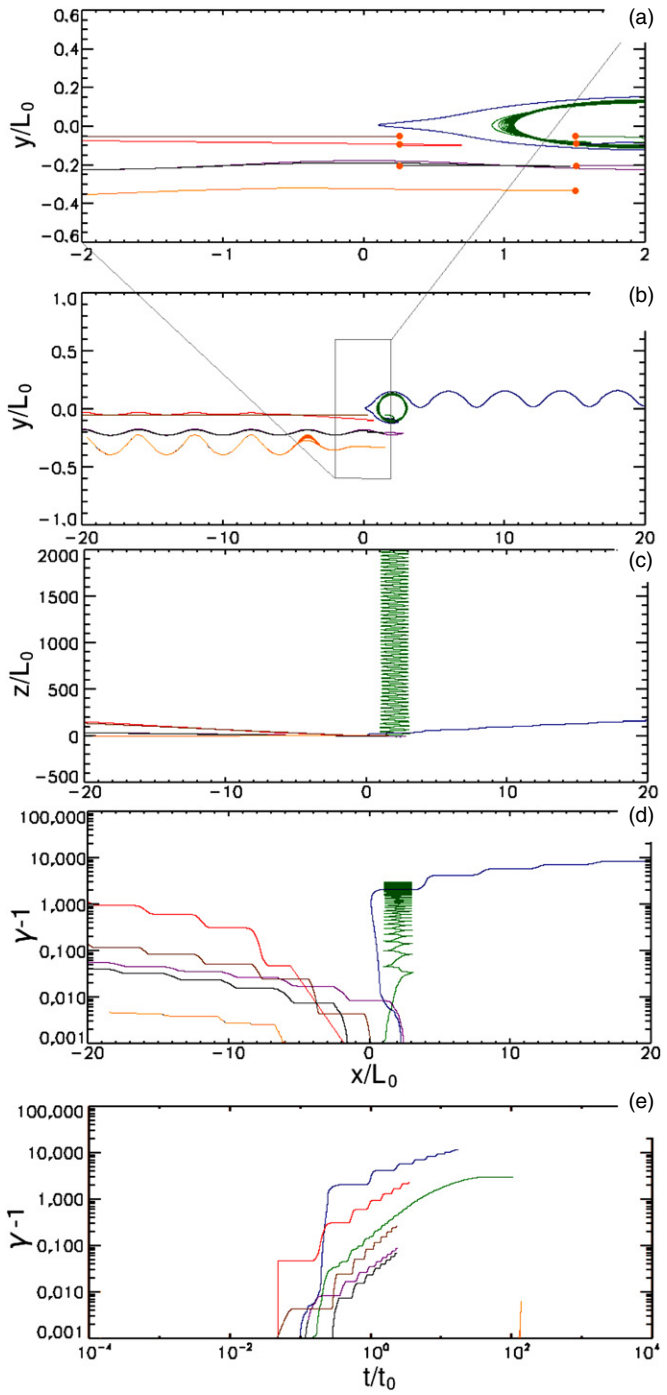

Figure 5. Same as Figure 4 but for electrons with initial parallel velocity $v_{||} = 4.0\,v_0$.

(A color version of this figure is available in the online journal.)

they are accelerated not only by the strong electric field in the vicinity of the X-point but also by a weaker electric field concentrated around magnetic islands. Finally, the presence of an electric field and guiding magnetic field causes asymmetry in proton and electron directions: electrons in $y > 0$ semispace have positive v_x components and negative v_x components in $y < 0$ semispace, while protons move in opposite directions.

3.3. Particle Energy Spectra

The particle kinetic energy is calculated as $E = mc^2(\gamma - 1)$. The temporal evolution of the proton and electron spectra

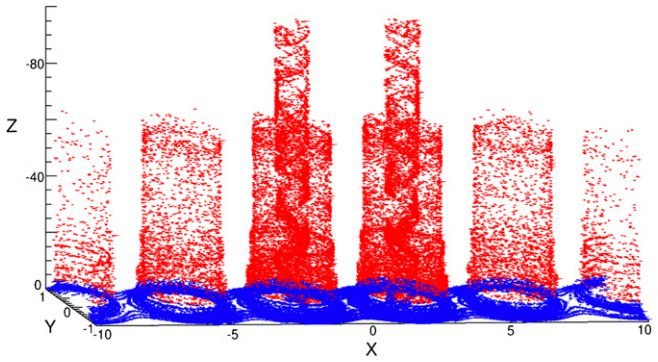

Figure 6. Proton distribution in space at the end of reconnection. Red crosses denote protons with high z-velocities $|v_z| > 0.5\,v_0$, while blue triangles denote particles with low z-velocities. It should be noted that all the protons have negative z-velocity. In these simulations, the magnetic and electric field are taken from the model with $y_0 = 0.25\,L_0$ and $\eta_1 = 3.2 \times 10^{-4}\,\mu_0 L_0 v_0$.

(A color version of this figure is available in the online journal.)

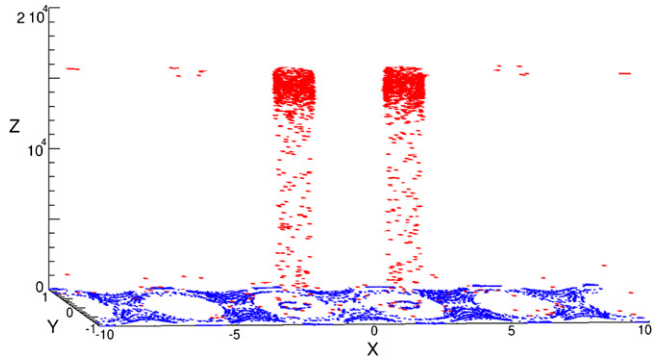

Figure 7. Same as Figure 6 but for electrons. Red crosses denote particles with high z-velocities $|v_z| > 10\,v_0$, while blue triangles denote particles with low z-velocities.

(A color version of this figure is available in the online journal.)

for one of the considered models is shown in Figures 8 and 9, respectively. Generally, the electron and proton energy spectra have similar shapes: most particles remain within the Maxwellian thermal bump while a small number get into a high-energy tail (Paper I 2010). However, there are noticeable differences, especially during the early stages of the RCS evolution.

The spectra evolve while the magnetic reconnection occurs. During the X-point stage of RCS evolution the electric field is strong and particles (both protons and electrons) are accelerated up to energies of ~1–10 MeV. It is interesting to note the depression in the electron energy spectrum during this stage between ~1 and ~40 keV. Most likely this gap is due to the "step-like" resistivity function chosen in the MHD model. Indeed, the diffusion region where the $\eta\vec{j}$ component of electric field is non-zero should have a rather sharp edge. As a result, particles that get into this region gain significant energy while the remaining particles maintain their initial thermal energy. The gradual decrease in the current density (and, therefore, in electric field strength) leads to acceleration of electrons to lower energies and the gap is filled, so that at the end of reconnection, the electron energy spectrum is a monotonic function. The reason why protons do not reveal such a depression in their energy spectra is most likely due to their long acceleration time. Indeed, the proton acceleration time is $\sim 10 t_0$ (compared to $< 1 t_0$ for electrons) which is not much smaller than the characteristic time of magnetic reconnection ($\sim 100 t_0$, see Paper I). Therefore,

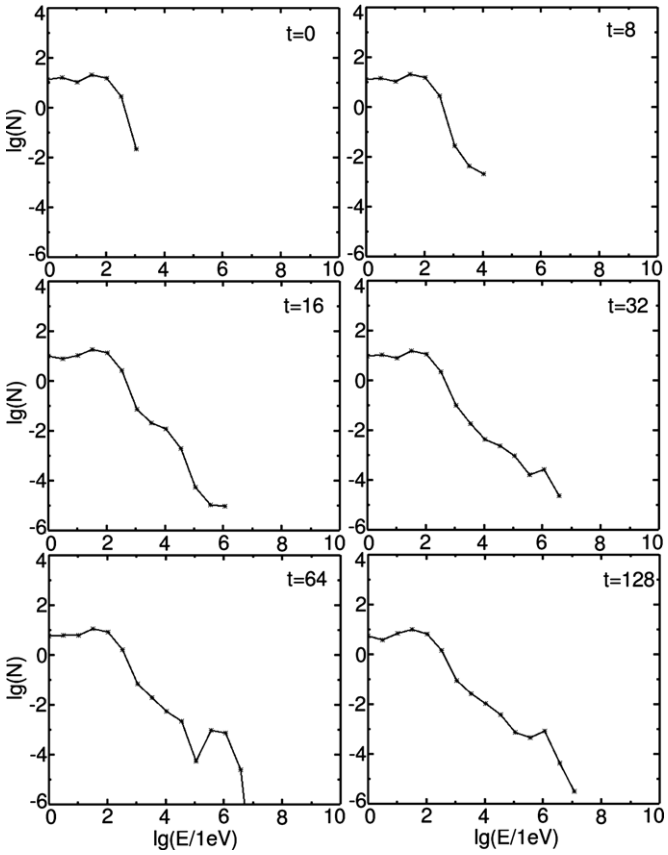

Figure 8. Variation of the proton energy spectra during magnetic reconnection in the model with $y_0 = 0.25\,L_0$ and $\eta_1 = 3.2 \times 10^{-4}\,\mu_0 L_0 v_0$. Corresponding time values (normalized by t_0) are shown in the panels.

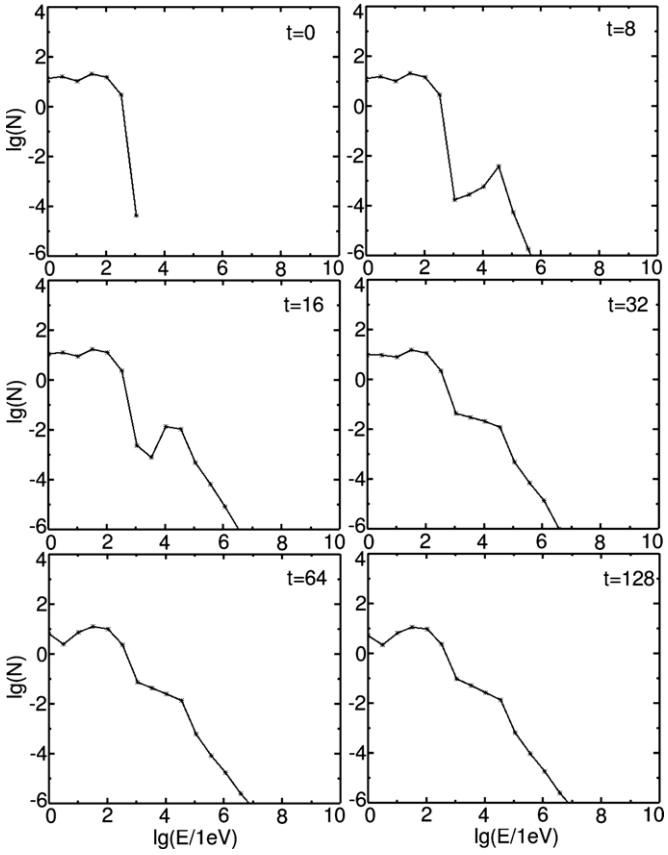

Figure 9. Same as Figure 8 but for electrons.

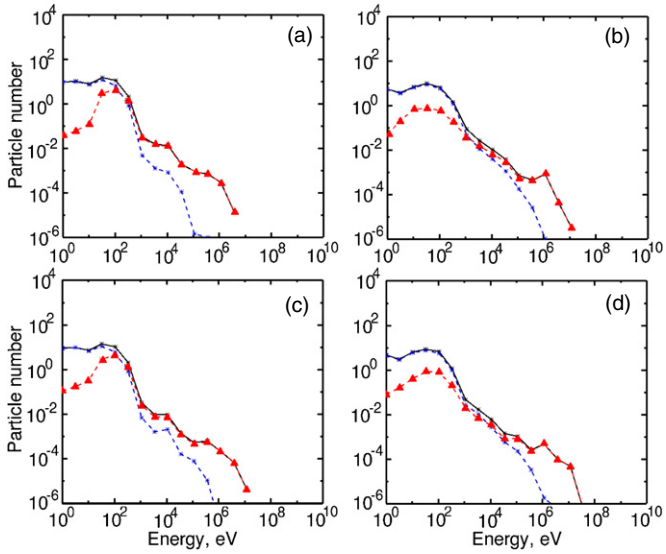

Figure 10. Energy spectra at the end of reconnection. Dashed lines with stars correspond to the open field protons, dashed lines with triangles correspond to protons trapped in closed field. Black solid lines denotes the total spectra. Panels (a–b) and (c–d) are for $\eta_1 = 3.2 \times 10^{-4}\,\mu_0 L_0 v_0$ and $\eta_1 = 3.2 \times 10^{-3}\,\mu_0 L_0 v_0$, respectively. Panels (a) and (c) are for the CS characteristic width $y_0 = 0.4\,L_0$, panels (b) and (d) are for $y_0 = 0.25\,L_0$.

(A color version of this figure is available in the online journal.)

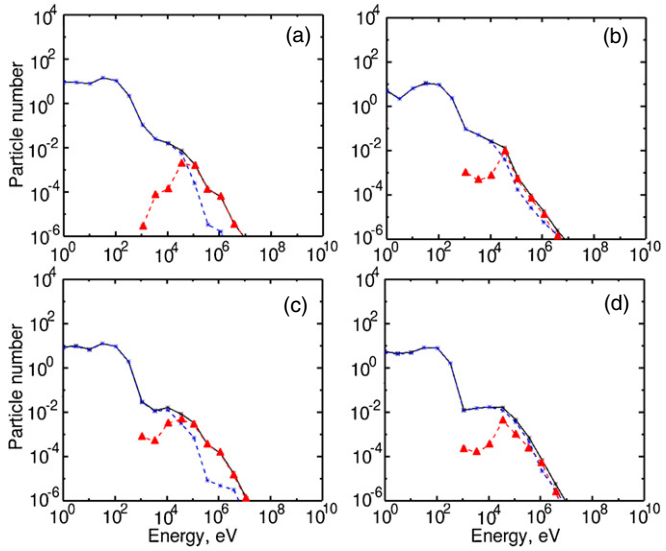

Figure 11. Same as Figure 10 but for electrons.

(A color version of this figure is available in the online journal.)

the electric field in the diffusion region may change during a particle acceleration and this effect leads to the smoother energy spectrum.

Analysis of particle energies also shows the existence of two populations. It can be seen from the final energy spectra (Figures 10 and 11) that particles trapped in the islands with closed magnetic field have on average much higher energies. Thus, the trapped proton "test particles" have energies of up to 10–100 MeV while those traveling in open field are accelerated only up to ∼1 MeV. At the same time, the number of thermal particles in the magnetic islands is smaller by a factor ∼10–100 than number of the thermal particles in the open field. This effect is even more noticeable in the electron spectra. It can be seen that thermal particles are practically absent in the trapped electron population. At the same time, the high-energy parts

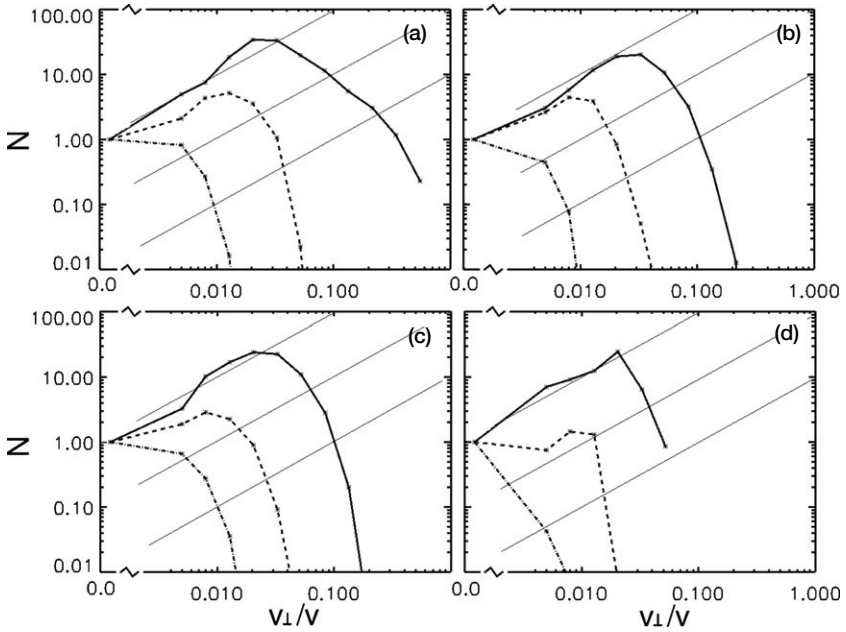

Figure 12. Pitch-angular distribution of test particles (arbitrary normalization). Panels (a) and (b) are for protons, panels (c) and (d) are for electrons. Panels (a) and (c) are for particles in open magnetic field, panels (b) and (c) are for the magnetic island particles. Solid lines are for energy range 10–100 keV, dashed lines are for 100 keV–1 MeV, and dot-dashed lines are for >1 MeV. For comparison, thin blue lines show the pitch-angular distribution for the fully isotropic case.

for electrons in open and closed field lines are rather similar. These discrepancies between the manifestations of different populations in electrons and protons also appear, most likely, due to the difference in average proton and electron acceleration times.

The spectral indices γ ($N \sim E^{-\gamma}$) in the high-energy parts of these spectra are similar to those obtained in Paper I. At the end of reconnection the electron energy spectra between 10 keV and 1 MeV show indices of $\gamma \sim 2.0$. The proton spectra are harder with $\gamma \sim 1.0$–1.5 at $E \sim 1$ MeV.

3.4. Pitch-angular Distribution

Final test-particle distributions over pitch-angle sine ($\sin\theta = \sqrt{u_g^2+u^2}/\sqrt{u_g^2+u^2+v_{||}^2}$) are shown in Figure 12. It can be seen that, in general, particles move predominantly along the field lines. High-energy electrons show better collimation to the magnetic field lines than protons: depending on energy the widths of their θ distributions is by factor ~2–10 smaller than those of electrons.

Both particle species show narrower pitch-angle distributions for higher energy. This effect can be easily explained taking into account that the particles are accelerated mostly along the magnetic field by the parallel electric field while gyro-velocities remain nearly unchanged and the $E \times B$ drift velocities should be negligible after the reconnection ends. Therefore, the average pitch angle should depend on energies approximately as $\sim E^{-1/2}$.

Finally, it is interesting to note that, while the two particle populations have similar pitch-angle distributions, the protons and electrons moving around O-points (Figure 12(b)) have noticeably narrower distributions.

4. DISCUSSION AND CONCLUSIONS

There are many effects that could lead to a magnetic reconnection event in a fragmenting CS as described in Section 2.

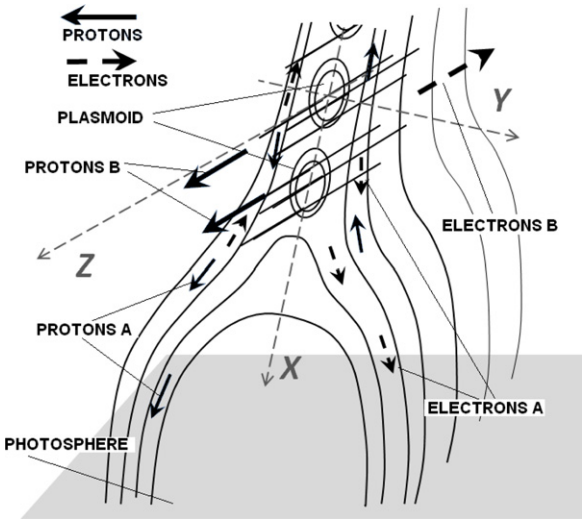

Figure 13. Proton and electron motion in a fragmented CS occurring in the flaring arcade. Open field particles are designated as population A, magnetic island particles are designated as population B.

MHD waves, which are ubiquitous in the magnetically dominated solar corona, or deformation of the magnetic field due to the photospheric footpoint motion can easily cause a magnetic field perturbation similar to that used in our MHD model to trigger the magnetic reconnection (see, e.g., Kusano et al. 2004; Inglis & Nakariakov 2009; Tripathi et al. 2009). This scenario also is supported by some recent observations of externally triggered explosive events (Jess et al. 2010). On the other hand, the initial Harris CS configuration (Equation (1)) itself can be unstable to the tearing mode (see, e.g., Lottermoser & Scholer 1997) with a wavelength larger than the initial CS thickness y_0. Hence, the reconnection considered in Section 2 can occur without an external driver. In terms of coronal geometry, the considered model can represent fragmentation of non-neutral CS in a coronal arcade with formation of plasmoids (Figure 13;

see also Magara et al. 1997; Barta et al. 2009). Let us discuss the implications for the particle motion based on this geometric model.

The first population of accelerated particles (*protons A* and *electrons A* in Figure 13) move in the open magnetic field. Due to the presence of a guiding field (B_z) protons and electrons precipitate asymmetrically with respect to the initial CS mid-plane (x–z) (see Zharkova & Gordovskyy 2004; Paper I), i.e., high-energy protons precipitate predominantly toward the left footpoint (or flare ribbon) while electrons precipitate toward the right footpoint (or flare ribbon). As far as the trapped particles (*protons B* and *electrons B*) are concerned they move within the magnetic islands (or plasmoids) predominantly along the guiding field B_z. However, this particle population also shows proton/electron asymmetry: all the accelerated electrons have positive v_z velocity components while all the protons have negative v_z components.

Naturally, such a proton and electron separation should induce an electric field which may significantly affect the evolution of the CS and the particle acceleration (Siversky & Zharkova 2009). This effect is not taken into account here and, therefore, the present model is not fully self-consistent. Generally, if the number of accelerated particles is small compared to the total particle number, the induced electric field can be easily compensated for by the current of thermal electrons (the so-called return current, see, e.g., Emslie 1981; Diakonov & Somov 1988; Siniavskii & Zharkova 1994) and, hence, it should not substantially affect the reconnection and acceleration model. However, there is an obvious need for a self-consistent model in order to study the self-induced electric field effect.

This work is supported by the Science and Technology Facilities Council (UK), grant ST/F003064/1. We are grateful to Tony Arber (University of Warwick) for use of the Lare2d code.

REFERENCES

Arber, T. D., Longbottom, A. W., Gerrard, C. L., & Milne, M. 2001, J. Comput. Phys., 171, 151
Aschwanden, M. J. 2002, Space Sci. Rev., 101, 1
Barta, M., Buchner, J., & Karlicky, M. 2009, Adv. Space Res., 45, 10
Benz, A. O. 2008, Liv. Rev. Sol. Phys., 5, 1
Diakonov, S. V., & Somov, B. V. 1988, Sol. Phys., 116, 119
Dreher, J., Birk, G. T., & Neukirch, T. 1997, A&A, 323, 593
Emslie, A. G. 1981, ApJ, 249, 817
Gordovskyy, M., Browning, P. K., & Vekstein, G. E. 2010, A&A, in press (Paper I)
Hahm, T. S., & Kulsrud, R. M. 1985, Phys. Fluids, 28, 2412
Heerikhuisen, J., Litvinenko, Yu. E., & Craig, I. J. D. 2002, ApJ, 566, 512
Inglis, A. R., & Nakariakov, V. M. 2009, A&A, 492, 259
Jain, R., Browning, P. K., & Kusano, K. 2005, Phys. Plasmas, 12, 012904
Jess, D. B., Mathioudakis, M., Browning, P. K., Crockett, P. J., & Keenan, F. P. 2010, ApJ, 712, L111
Klein, K.-L., & MacKinnon, A. 2007, Lect. Notes Phys., 725, 1
Kliem, B. 1994, ApJS, 90, 719
Kusano, K., Maeshiro, T., Yokoyama, T., & Sakurai, T. 2004, ApJ, 610, 537
Lin, R. P. 2008, AIP Conf. Proc. 1039, Particle Acceleration and Transport in the Heliosphere and Beyond (Melville, NY: AIP), 52
Litvinenko, Yu. E., & Somov, B. V. 1993, Sol. Phys., 146, 127
Lottermoser, R.-F., & Scholer, M. 1997, J. Geophys. Res., 102, 4875
Magara, T., Shibata, K., & Yokoyama, T. 1997, ApJ, 487, 437
Martens, P. C. H., & Young, A. 1990, ApJS, 73, 333
Northrop, T. 1963, The Adiabatic Motion of Charged Particles (Wiley, NY: Interscience), 109
Oka, M., Phan, T.-D., Krucker, S., Fujimoto, M., & Shinohara, I. 2010, ApJ, 714, 915
Priest, E. R. 1982, Solar Magnetohydrodynamics (Dordrecht: Reidel)
Sato, T., Matsumoto, H., & Nagai, K. 1982, J. Geophys. Res., 87, 6089
Siniavskii, D. V., & Zharkova, V. V. 1994, ApJS, 90, 729
Siversky, T. V., & Zharkova, V. V. 2009, J. Plasma Phys., 75, 619
Speiser, T. W. 1965, J. Geophys. Res., 70, 4219
Tripathi, D., Isobe, H., & Jain, R. 2009, Space Sci. Rev., 149, 283
Vekstein, G. E., & Jain, R. 1998, Phys. Plasmas, 5, 1506
Vlahos, L., Krucker, S., & Cargill, P. 2009, Lect. Notes Phys., 778, 157
Wood, P., & Neukirch, T. 2005, Sol. Phys., 226, 73
Zharkova, V. V., & Gordovskyy, M. 2004, ApJ, 604, 884
Zhu, Z., & Parks, G. 1993, J. Geophys. Res., 98, 7603